



# Experimental evidence of low-density liquid water upon rapid decompression

Chuanlong Lin<sup>a</sup>, Jesse S. Smith<sup>a</sup>, Stanislav V. Sinogeikin<sup>a</sup>, and Guoyin Shen<sup>a,1</sup>

<sup>a</sup>High Pressure Collaborative Access Team, Geophysical Laboratory, Carnegie Institution of Washington, Argonne, IL 60439

Edited by Pablo G. Debenedetti, Princeton University, Princeton, NJ, and approved January 19, 2018 (received for review September 15, 2017)

**Water is an extraordinary liquid, having a number of anomalous properties which become strongly enhanced in the supercooled region. Due to rapid crystallization of supercooled water, there exists a region that has been experimentally inaccessible for studying deeply supercooled bulk water. Using a rapid decompression technique integrated with in situ X-ray diffraction, we show that a high-pressure ice phase transforms to a low-density noncrystalline (LDN) form upon rapid release of pressure at temperatures of 140–165 K. The LDN subsequently crystallizes into ice- $I_c$  through a diffusion-controlled process. Together with the change in crystallization rate with temperature, the experimental evidence indicates that the LDN is a low-density liquid (LDL). The measured X-ray diffraction data show that the LDL is tetrahedrally coordinated with the tetrahedral network fully developed and clearly linked to low-density amorphous ices. On the other hand, there is a distinct difference in structure between the LDL and supercooled water or liquid water in terms of the tetrahedral order parameter.**

low-density liquid | rapid decompression | low-density amorphous ice | time-resolved X-ray diffraction

**W**ater is not only the most important substance for life, but also plays important roles in liquid science for its anomalous properties (1–6). For instance, water displays minima of isobaric heat capacity at 308 K and isothermal compressibility at 319 K which are related to entropy and density fluctuations, respectively (2–6). It has been widely accepted that water’s anomalies are not a result of simple thermal fluctuation, but are connected to the formation of various structural aggregates in the hydrogen bonding network (4, 7). Among several proposed scenarios (1, 2, 6–16), one model of fluctuations between two different liquids has gradually gained traction (4, 7–9, 14, 17–26). These two liquids are referred to as a low-density liquid (LDL) and a high-density liquid (HDL) with a coexistence line in the deeply supercooled regime at elevated pressure (8, 14). The LDL–HDL transition ends with decreasing pressure at a liquid–liquid critical point (LLCP) (8, 14) with its Widom line extending to low pressures (1, 27) (*SI Appendix, Fig. S1*). Above the Widom line lies mostly HDL which is favored by entropy, while LDL, mostly lying below the Widom line, is favored by enthalpy in the tetrahedral hydrogen bonding network. The origin of water’s anomalies can then be explained by the increase in structural fluctuations (7, 15) as water is cooled down to deeply supercooled temperatures approaching the Widom line.

However, both the LLCP and the LDL–HDL transition line lie in water’s “no man’s land” between the homogeneous nucleation temperature ( $T_H$ , ~232 K) (28, 29) and the crystallization temperature ( $T_X$ , ~150 K) (30–33). The success of experiments exploring this region has been limited thus far, despite various attempts made to probe supercooled water either by rapidly supercooling bulk water below  $T_H$  (29) or by heating amorphous ices near  $T_X$  (31–35), as well as other methods using aqueous solutions (36, 37) and confined water systems (19, 21, 22, 38–41). For instance, Mishima and Stanley observed a discontinuous melting in the studies of the metastable melting curves of high-pressure emulsified ices (IV, III, and V) and pointed out that there may be an LLCP at around 110 MPa and 220 K (14, 19, 21). However, the starting emulsified ices, made by stirring a mixture of

water, methylcyclohexane, methylcyclopentane, and sorbitan tris-terate (21), may have different physical properties from those of bulk water (42). Recently, ultrafast X-ray pulse has been used to probe supercooled bulk water down to 227 K (29), 5 K below the previous boundary of  $T_H$ , showing a continuous and accelerating increase in structural ordering as temperature is decreased. On the low-temperature side by heating amorphous ices above the glass transition temperature ( $T_g$ ), experiments have shown evidence of a deeply supercooled water near  $T_g$  (31–35, 43, 44). At temperatures below  $T_g$ , there exist two kinds of amorphous ices, low-density amorphous (LDA) and high-density amorphous (HDA), with two phases transforming to each other through a first-order-like transition (14, 30, 45–49). At temperatures well above  $T_g$ , the heating approach becomes limited due to uncontrolled crystallization. Xu et al. (50) recently used a pulsed laser heating technique and measured the isothermal growth rate of crystalline ice at temperatures of 126–151 K and above 180 K, but leaving no data between 151 and 180 K. More experiments are thus needed to better understand the nature of both the structure and the crystallization process of the deeply supercooled water at temperatures above  $T_g$ . In this work, we apply a rapid decompression technique (51) integrated with fast in situ X-ray diffraction (*Materials and Methods*). We find that a high-pressure phase ice-VIII transforms to a low-density noncrystalline (LDN) form under rapid and complete release of pressure at 140–165 K. We record the crystallization process under vacuum (3–5 mtorr) in a cryostat using the time-resolved X-ray diffraction as the LDN subsequently crystallizes into ice- $I_c$ .

## Significance

To understand water’s anomalous behavior, a two-liquid model with a high-density liquid and a low-density liquid (LDL) has been proposed from theoretical simulations, and is gradually gaining ground. However, it has been experimentally challenging to probe the region of the phase diagram of H<sub>2</sub>O where the LDL phase is expected to occur. We overcome the experimental challenge by using a technique of rapid decompression integrated with fast synchrotron measurements, and show that the region of LDL is accessible via decompression of a high-pressure crystal. We report the experimental evidence of the LDL from in situ X-ray diffraction and its crystallization process, providing a kinetic pathway for the appearance of LDL as an intermediate phase in the crystal–crystal transformation upon decompression.

Author contributions: C.L. and G.S. designed research; C.L., J.S.S., and S.V.S. performed research; C.L. analyzed data; C.L. and G.S. interpreted data; and C.L. and G.S. wrote the paper.

The authors declare no conflict of interest.

This article is a PNAS Direct Submission.

This open access article is distributed under [Creative Commons Attribution-NonCommercial-NoDerivatives License 4.0 \(CC BY-NC-ND\)](https://creativecommons.org/licenses/by-nc-nd/4.0/).

<sup>1</sup>To whom correspondence should be addressed. Email: [gshen@ciw.edu](mailto:gshen@ciw.edu).

This article contains supporting information online at [www.pnas.org/lookup/suppl/doi:10.1073/pnas.1716310115/-DCSupplemental](http://www.pnas.org/lookup/suppl/doi:10.1073/pnas.1716310115/-DCSupplemental).

Published online February 12, 2018.



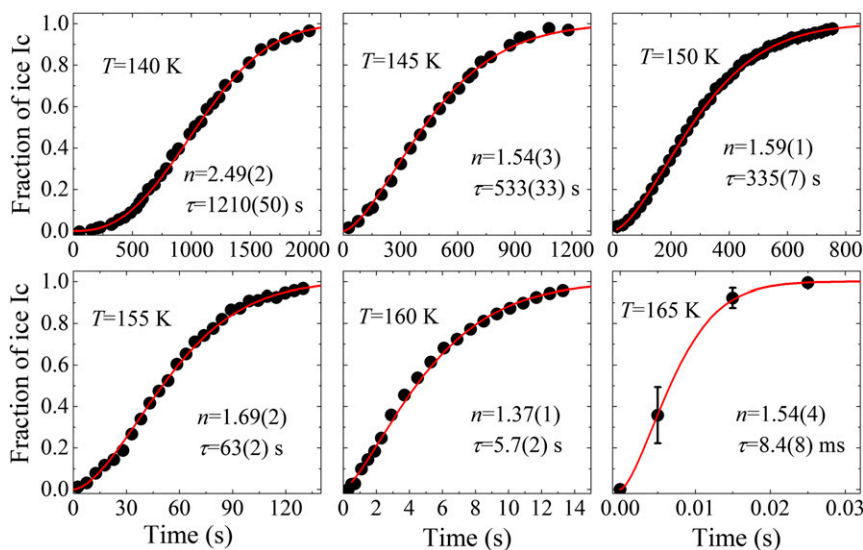


**Fig. 2.** Transformed fractions of ice-I<sub>c</sub> as a function of time at ~3–5 mtorr between 140 and 165 K. Black circles show the experimental data from the intensities of X-ray diffraction. Red lines are the fitting results using the Avrami equation, with the Avrami index ( $n$ ) and the characteristic time ( $\tau$ ) shown in each figure.

current time resolution (at a few milliseconds) in our X-ray diffraction measurements. At the highest temperature of 175 K in this study, ice-VIII is found to transform to ice-VI at a decompression rate of ~48 GPa/s, followed by the transformation to ice-II and I<sub>c</sub> (*SI Appendix*, Fig. S8). Fig. 1D shows the integrated diffraction patterns with background subtracted (*Materials and Methods* and *SI Appendix*, Fig. S9), compared with those of LDA and HDA. The LDA sample at 125 K was obtained by first forming HDA under high pressure (~2 GPa) and then decompressing the HDA at 125 K via an HDA–LDA transformation. The LDA sample at 103 K was obtained by cooling the LDA sample from 125 to 103 K. The HDA sample at 96 K was obtained by first compressing ice-I<sub>h</sub> at 96 K to ~2 GPa and then decompressing the formed HDA to vacuum pressure (52). It can be clearly seen that the diffraction patterns of the noncrystalline phase are similar to those of LDA, indicating that it is an LDN phase transformed from ice-VIII under rapid decompression.

Fig. 2 shows the fractions of ice-I<sub>c</sub> transformed from the LDN plotted against time ( $t$ ) between 140 and 165 K and at 3–5 mtorr. The fractions are calculated using the diffraction intensities of ice-I<sub>c</sub> (*Materials and Methods* and *SI Appendix*, Fig. S10). At a given  $T$ , the fraction gives a typical sigmoidal curve as a function of time. The sigmoidal patterns can be well-fitted using the Avrami equation (55–57):  $f(t) = 1 - \exp[-(t/\tau)^n]$ , where  $\tau$  is the characteristic time of the crystallization and  $n$  is the dimensionality of the crystal growth, also referred to as the Avrami index. The index  $n$  generally reflects the growth mechanism, with integer  $n$  corresponding to interface-controlled growth and half-integer  $n$  (1/2, 3/2, 5/2, ...) corresponding to diffusion-controlled growth (55, 57, 58). As shown in Fig. 2, the fittings yield  $n$  values close to half-integer of the Avrami index, indicating that the growth of ice-I<sub>c</sub> transformed from the LDN is via a diffusion-controlled mechanism. Given that the temperature range of the observed LDN is above  $T_g$  of 136 K (31, 54, 59, 60), the crystallization mechanism suggests that the LDN is of liquid-like nature. It should be noted that  $n$  values are close to 1.5 at  $T > 140$  K, corresponding to diffusion-controlled growth of spherical nuclei in the case of rapid nucleation rate and depletion (61, 62). At 140 K,  $n$  is close to 2.5, which may be due to a relatively long nucleation duration (62, 63).

The temperature dependence of the crystallization rate (rate constant:  $\sim 1/\tau$ ) provides further evidence that the LDN is an LDL. According to classical nucleation and growth theory, the growth rate ( $v$ ) in a diffusion-controlled process is determined by the diffusion coefficient ( $D$ ) with a relationship (55):  $v \sim \sqrt{D/t}$ . The Arrhenius behavior of the diffusion coefficient can be indicated by the temperature dependence of the characteristic time (55). Fig. 3 shows the logarithm of the characteristic time as a function of temperature. It is clear that in the covered range of 140–165 K the crystallization displays non-Arrhenius behavior with at least two distinct regions. Below ~155 K,  $\log(\tau)$  has a linear relationship with inverse temperature, which is consistent with the results of previous studies using Fourier transform

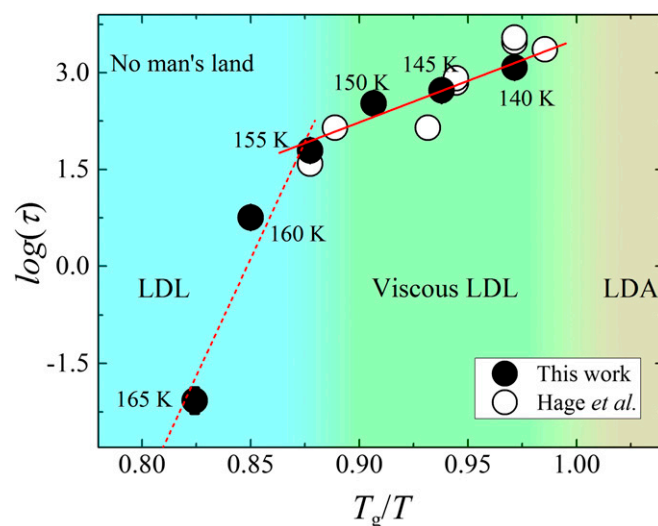


**Fig. 3.** Temperature dependence of the characteristic time ( $\tau$ , in seconds) for the crystallization of ice-I<sub>c</sub>. Inverse temperature relative to  $T_g$  (136 K) is used (28, 50). Solid circles are  $\tau$ -values from experimental data as shown in Fig. 2. Solid and dashed lines represent Arrhenius fittings with a kink at ~155 K. Open circles indicate the results by Hage *et al.* (62, 64), which were obtained by the crystallization kinetics of a hyperquenched glass upon warming.

infrared spectroscopy (62, 64). Such Arrhenius behavior implies that it could be a strong liquid at  $T$  between  $T_g$  and 155 K (22, 40, 42, 65–70). Fitting  $\tau$ - $T$  data according to the Arrhenius equation  $\tau = \tau_0 \exp(Q/RT)$ , where  $Q$  is the activation energy and  $R$  is the gas constant, yields an activation energy of 33(7) kJ/mol with  $\tau_0$  of  $4.4 \times 10^{-10}$  s. The activation energy is close to that of 34 kJ/mol from the structural relaxation of LDL obtained from dielectric spectroscopy (44). Above 155 K, we have limited data points and therefore cannot draw any conclusions as to whether the liquid above 155 K is a fragile or strong liquid (22, 40, 41, 65, 68). We tentatively fit the data according to the Arrhenius equation, yielding  $Q$  of 167(48) kJ/mol and  $\tau_0$  of  $3.6 \times 10^{-62}$  s. We note a recent report on the isothermal growth rate that exhibits a slope change in Arrhenius behavior with activation energies of  $\sim 47$  kJ/mol and  $\sim 76$  kJ/mol at  $T$  below 151 K and at  $T$  of 180–235 K, respectively (50). These values qualitatively agree with the activation energies in this study below and above the kink temperature, but slightly differ in values. This may be partly explained by the fact that the nucleation rate and the growth rate have not been independently determined in the present work and the crystallization rate cannot be directly compared with the growth rate (50).

Two possible mechanisms are considered to elucidate the kink at around 155 K. (i) The kink could be a reflection of the decoupling of self-diffusion from structural relaxation (71). According to the mode-coupling theory (MCT), there exists a critical temperature  $T_c$  for supercooled liquids, with diffusion mechanism changing from liquid-like motion to solid-like hopping (72–74).  $T_c$  in MCT is generally different from, and higher than, the caloric temperature  $T_g$ , with  $T_c$  close to  $1.2T_g$  for many fragile liquids (72, 75–78). From Fig. 3, the small activation energy below the kink temperature (155 K) could be related to the decoupling of translational diffusion from structural relaxation, whereas the large activation energy above 155 K reflects the effect of structural relaxation and represents the intrinsic property of a supercooled liquid state (72, 76, 79, 80). Similar kinks in the temperature-dependent diffusion coefficient have been observed in metallic glasses near the glass-transition temperatures (81–85). (ii) The kink at  $\sim 155$  K might be a signature of a fragile–strong dynamic cross-over (22, 40, 66–68). It should be noted that, due to the limited data points above 155 K, a fitting of our data to a Vogel–Fulcher–Tammann law remains ambiguous. It is thus inconclusive from our data alone to support a fragile–strong cross-over. It has been reported that there is a fragile–strong cross-over at  $\sim 220$  K from studies of confining water in nanopores (22, 40, 67, 70). Our kink temperature is  $\sim 65^\circ$  below the reported values. However, this discrepancy in temperature might be related to interaction of water molecules with the confining surfaces in these experiments (42). Regardless of which one of the above two mechanisms is responsible for the kink, the change in crystallization rate with temperature (Fig. 3) strongly supports the notion that the observed LDN is an LDL. Therefore, we indicate several regions in Fig. 3, with LDA ices lying below  $T_g$ , a viscous LDL at 136–155 K, and an LDL at 155–165 K.

## Discussion

The appearance of an LDL under rapid decompression is consistent with a recently proposed two-step phase-transition mechanism (86–88). In a solid–solid phase transition, a metastable liquid may appear first as an intermediate state before subsequently transforming to the stable product phase. The occurrence of an intermediate liquid is attributed to a much smaller interfacial energy barrier at the solid/liquid interface than that at the solid/solid interface (86). Such intermediate metastable liquid in solid–solid transitions has been experimentally observed in colloidal systems (86), metallic alloys (89), and an elemental metal (90). In our case for ice, such intermediate

phase is LDL, forming from the parent solid phase (ice-VIII) under rapid release of pressure, followed by the crystallization of the product solid (ice-I<sub>c</sub>).

How is the LDL structurally related to amorphous ices and supercooled water above  $T_H$ ? From X-ray scattering data (Fig. 1D), we plot the position of the first peak ( $Q_1$ ) and the peak separation between the first and the second peaks ( $\Delta Q = Q_2 - Q_1$ ) (Fig. 4), together with those data for LDA, supercooled water, and liquid water up to 360 K (29, 91). We can see that the structure of LDL reflected by  $Q_1$  and  $\Delta Q$  is similar to that of LDA (92–94), but is distinctly different from those of supercooled water and liquid water. As temperature gets down into the deeply supercooled region, both  $Q_1$  and  $\Delta Q$  for supercooled water display strong temperature dependences and change continuously, approaching values corresponding to tetrahedral structures (29, 95). In contrast, only weak temperature dependences of  $Q_1$  and  $\Delta Q$  are shown for LDL. Because  $\Delta Q$  is associated with the degree of tetrahedral configurations favored by water's directional hydrogen bonds (29), the trend in Fig. 4 suggests that the local tetrahedrally coordinated network is fully developed in LDL.

The relationship of LDA, LDL, and supercooled liquid can be used to explain water's anomalous properties. At high temperatures above  $\sim 319$  K (46 °C), water exhibits normal liquid behavior (dominated by HDL), in that both heat capacity and compressibility increase as it is heated (7). As water is cooled from 319 K down to supercooled temperatures, the structural fluctuations between LDL and HDL may cause the anomalous properties of water (4, 7, 8, 14). The anomalous region with structural fluctuations may extend down to around the Widom line. At temperatures far below the Widom line, water may exhibit normal liquid again dominated by the fully developed tetrahedrally structured LDL observed in this study.

## Materials and Methods

**Sample Preparation.** Symmetric diamond-anvil cells (DACs) with 400–500- $\mu\text{m}$  anvil culets were used for high-pressure experiments in a cryostat. Rhenium gaskets with an initial thickness of 250  $\mu\text{m}$  were preindented to a thickness

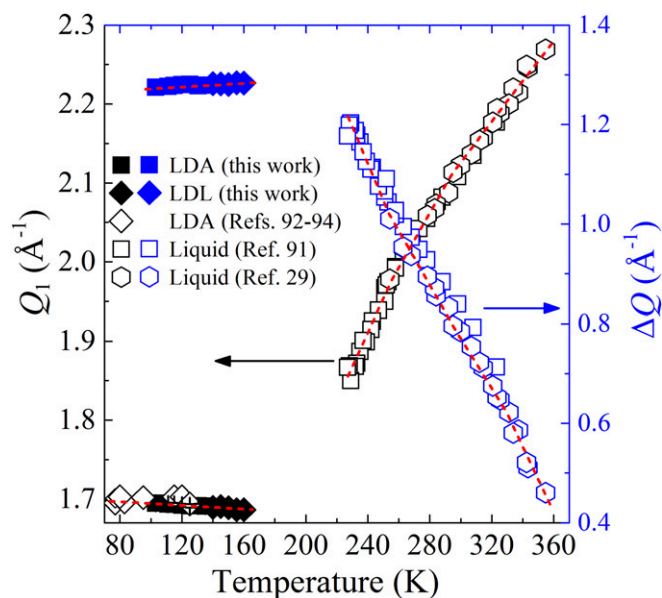


**Fig. 4.** Temperature dependences of the first peak position ( $Q_1$ , black) and the peak separation ( $\Delta Q$ , blue) between the first and second peaks in structure factor. Red dashed lines are a guide for the eyes. The data points for liquid water above 220 K are from refs. 29 and 91. Open diamonds for LDA are from refs. 92–94.

of  $\sim 100$   $\mu\text{m}$ . Sample holes with a diameter of  $\sim 200$   $\mu\text{m}$  were drilled by laser at the center of the indented area (96). Distilled deionized water was used and loaded into the sample chamber with a mass of  $\sim 1.7$   $\mu\text{g}$ , together with two or three ruby spheres located near the center and near the edge of the sample chambers (*SI Appendix, Fig. S9*). The pressures before and after rapid pressure ramps were determined by the ruby fluorescence method with temperature corrections (97, 98).

**Low-Temperature and Pressure Controls.** Loaded DACs were placed in a liquid nitrogen cryostat (99). Two silicon diode sensors were used to monitor the temperatures with one attached to the DAC holder and the other attached to the gasket close to the sample position. The sample temperature was monitored by the thermal sensor attached to the gasket. Before cooling, the pressure of the cryostat assembly was vacuum-pumped to 3–5 mtorr. The entire DAC assembly was then cooled using liquid nitrogen. A heater mounted on the holder allows the controls of DAC temperature precisely. The sample temperature was stable within  $\pm 2$  K during the experiments. Double-sided gas membranes were used to control compression and decompression pathways (99). After rapid pressure release, the sample remained under the vacuum environment inside a cryostat assembly. Therefore, the pressure condition in our isothermal measurements was at 3–5 mtorr, rather than ambient pressure of  $10^5$  Pa. During the decompression processes, the sample positions were monitored by X-ray radiography and/or an online optical system. We found that the sample position may change slightly ( $< 5$   $\mu\text{m}$ ) during decompression, which is negligible compared with the sample chamber diameter of 150  $\mu\text{m}$ . Furthermore, the measurements of the crystallization were taken after complete release of pressure, with the sample position well maintaining its position.

**In Situ X-Ray Diffraction.** Angle-dispersive X-ray diffraction experiments were performed at beamline 16-ID-B, HPCAT (51) at the Advanced Photon Source,

Argonne National Laboratory. X-ray beam with a wavelength of 0.61992 or 0.40663  $\text{\AA}$  was focused into a  $5 \times 6$ - $\mu\text{m}^2$  (full width at half maximum) spot on the sample. Two-dimensional diffraction images were collected continuously throughout the decompression process with a PILATUS 1M-F detector. The typical exposure time was from 5 s to 7 ms, depending on decompression rate and temperature. Diffraction data were analyzed and integrated using the software Dioptas (100). In the background subtraction, we used a diffraction image of crystalline ice-VIII as background to obtain a clear diffraction pattern of the low-density noncrystalline phase and ice- $I_c$  (52).

**Calculation of the Fraction of Ice- $I_c$ .** At a given temperature, the crystallization process was monitored by time-resolved in situ X-ray diffraction. We found that the growing ice- $I_c$  is fine-powdered relative to the X-ray beam size in this study, producing continuous diffraction rings (*SI Appendix, Fig. S9*). Therefore, the relative intensities of the diffraction peaks of ice- $I_c$  are a good measure of the ice- $I_c$  content, and may be used to quantify the crystallization process as a function of time (*SI Appendix, Fig. S10*). Using the diffraction intensity of  $I_c$  after the crystallization is complete as a reference, the fraction of  $I_c$  during the crystallization was determined by the normalized intensities relative to the reference.

**ACKNOWLEDGMENTS.** We thank Curtis Kenney-Benson, Eric Rod, and Richard Ferry for technical support, and Russell Hemley for useful discussions. This research was supported by the Department of Energy (DOE), Office of Basic Energy Science, Division of Materials Sciences and Engineering under Award DE-FG02-99ER45775. High Pressure Collaborative Access Team operations are supported by DOE, National Nuclear Security Administration under Award DE-NA0001974. The Advanced Photon Source is a User Facility operated for the DOE Office of Science by Argonne National Laboratory under Contract DE-AC02-06CH11357.

- Amann-Winkel K, et al. (2016) Colloquium: Water's controversial glass transitions. *Rev Mod Phys* 88:011002.
- Gallo P, et al. (2016) Water: A tale of two liquids. *Chem Rev* 116:7463–7500.
- Angell CA, Oguni M, Sichina WJ (1982) Heat-capacity of water at extremes of supercooling and superheating. *J Phys Chem* 86:998–1002.
- Debenedetti PG, Stanley HE (2003) Supercooled and glassy water. *Phys Today* 56:40–46.
- Kanno H, Angell CA (1979) Water–Anomalous compressibilities to 1.9-kbar and correlation with supercooling limits. *J Chem Phys* 70:4008–4016.
- Speedy RJ, Angell CA (1976) Isothermal compressibility of supercooled water and evidence for a thermodynamic singularity at  $-45^\circ\text{C}$ . *J Chem Phys* 65:851–858.
- Nilson A, Pettersson LGM (2015) The structural origin of anomalous properties of liquid water. *Nat Commun* 6:8998.
- Poole PH, Sciortino F, Essmann U, Stanley HE (1992) Phase behavior of metastable water. *Nature* 360:324–328.
- Poole PH, Sciortino F, Grande T, Stanley HE, Angell CA (1994) Effect of hydrogen bonds on the thermodynamic behavior of liquid water. *Phys Rev Lett* 73:1632–1635.
- Speedy RJ (1982) Stability-limit conjecture—An interpretation of the properties of water. *J Phys Chem* 86:982–991.
- Tanaka H (2000) Simple physical model of liquid water. *J Chem Phys* 112:799–809.
- Fuentevilla DA, Anisimov MA (2006) Scaled equation of state for supercooled water near the liquid-liquid critical point. *Phys Rev Lett* 97:195702.
- Holten V, Anisimov MA (2012) Entropy-driven liquid-liquid separation in supercooled water. *Sci Rep* 2:713.
- Mishima O, Stanley HE (1998) The relationship between liquid, supercooled and glassy water. *Nature* 396:329–335.
- Xu L, et al. (2005) Relation between the Widom line and the dynamic crossover in systems with a liquid-liquid phase transition. *Proc Natl Acad Sci USA* 102:16558–16562.
- Limmer DT, Chandler D (2011) The putative liquid-liquid transition is a liquid-solid transition in atomistic models of water. *J Chem Phys* 135:134503.
- Ponyatovskii EG, Sinand VV, Pozdnyakova TA (1994) 2nd critical-point and low-temperature anomalies in the physical-properties of water. *JETP Lett* 60:360–364.
- Angell CA (2004) Amorphous water. *Annu Rev Phys Chem* 55:559–583.
- Mishima O, Stanley HE (1998) Decompression-induced melting of ice IV and the liquid-liquid transition in water. *Nature* 392:164–168.
- Sciortino F, La Nave E, Tartaglia P (2003) Physics of the liquid-liquid critical point. *Phys Rev Lett* 91:155701.
- Mishima O (2000) Liquid-liquid critical point in heavy water. *Phys Rev Lett* 85:334–336.
- Chen SH, et al. (2006) The violation of the Stokes-Einstein relation in supercooled water. *Proc Natl Acad Sci USA* 103:12974–12978.
- Giovambattista N, Loerting T, Lukanov BR, Starr FW (2012) Interplay of the glass transition and the liquid-liquid phase transition in water. *Sci Rep* 2:390.
- Palmer JC, et al. (2014) Metastable liquid-liquid transition in a molecular model of water. *Nature* 510:385–388.
- Smallenburg F, Sciortino F (2015) Tuning the liquid-liquid transition by modulating the hydrogen-bond angular flexibility in a model for water. *Phys Rev Lett* 115:015701.
- Ni Y, Skinner JL (2016) Evidence for a liquid-liquid critical point in supercooled water within the E3B3 model and a possible interpretation of the kink in the homogeneous nucleation line. *J Chem Phys* 144:214501.
- Russo J, Tanaka H (2014) Understanding water's anomalies with locally favoured structures. *Nat Commun* 5:3556.
- Mason BJ (1958) The supercooling and nucleation of water. *Adv Phys* 7:221–234.
- Sellberg JA, et al. (2014) Ultrafast X-ray probing of water structure below the homogeneous ice nucleation temperature. *Nature* 510:381–384.
- Mishima O (1994) Reversible first-order transition between two H<sub>2</sub>O amorphs at  $\sim 0.2$  GPa and  $\sim 135$  K. *J Chem Phys* 100:5910–5912.
- Johari GP, Hallbrucker A, Mayer E (1987) The glass liquid transition of hyperquenched water. *Nature* 330:552–553.
- Smith RS, Kay BD (1999) The existence of supercooled liquid water at 150 K. *Nature* 398:788–791.
- Andersson O (2011) Glass-liquid transition of water at high pressure. *Proc Natl Acad Sci USA* 108:11013–11016.
- Hill CR, et al. (2016) Neutron scattering analysis of water's glass transition and micropore collapse in amorphous solid water. *Phys Rev Lett* 116:215501.
- Perakis F, et al. (2017) Diffusive dynamics during the high-to-low density transition in amorphous ice. *Proc Natl Acad Sci USA* 114:8193–8198.
- Kim CU, Tate MW, Gruner SM (2015) Glass-to-cryogenic-liquid transitions in aqueous solutions suggested by crack healing. *Proc Natl Acad Sci USA* 112:11765–11770.
- Corradini D, Gallo P (2011) Liquid-liquid coexistence in NaCl aqueous solutions: A simulation study of concentration effects. *J Phys Chem B* 115:14161–14166.
- Cupane A, Fomina M, Piazza I, Peters J, Schirò G (2014) Experimental evidence for a liquid-liquid crossover in deeply cooled confined water. *Phys Rev Lett* 113:215701.
- Kim CU, Barstow B, Tate MW, Gruner SM (2009) Evidence for liquid water during the high-density to low-density amorphous ice transition. *Proc Natl Acad Sci USA* 106:4596–4600.
- Chen SH, et al. (2006) Observation of fragile-to-strong dynamic crossover in protein hydration water. *Proc Natl Acad Sci USA* 103:9012–9016.
- Kumar P (2006) Breakdown of the Stokes-Einstein relation in supercooled water. *Proc Natl Acad Sci USA* 103:12955–12956.
- Levinger NE (2002) Chemistry. Water in confinement. *Science* 298:1722–1723.
- Elsaesser MS, Winkel K, Mayer E, Loerting T (2010) Reversibility and isotope effect of the calorimetric glass  $\rightarrow$  liquid transition of low-density amorphous ice. *Phys Chem Chem Phys* 12:708–712.
- Amann-Winkel K, et al. (2013) Water's second glass transition. *Proc Natl Acad Sci USA* 110:17720–17725.
- Nelmes RJ, et al. (2006) Annealed high-density amorphous ice under pressure. *Nat Phys* 2:414–418.
- Klotz S, et al. (2005) Nature of the polyamorphic transition in ice under pressure. *Phys Rev Lett* 94:025506.

47. Mishima O, Suzuki Y (2002) Propagation of the polyamorphic transition of ice and the liquid-liquid critical point. *Nature* 419:599–603.
48. Mishima O, Calvert LD, Whalley E (1984) Melting ice-I at 77-K and 10-kbar—A new method of making amorphous solids. *Nature* 310:393–395.
49. Mishima O, Calvert LD, Whalley E (1985) An apparently 1st-order transition between 2 amorphous phases of ice induced by pressure. *Nature* 314:76–78.
50. Xu Y, Petrik NG, Smith RS, Kay BD, Kimmel GA (2016) Growth rate of crystalline ice and the diffusivity of supercooled water from 126 to 262 K. *Proc Natl Acad Sci USA* 113:14921–14925.
51. Smith JS, et al. (2015) Developments in time-resolved high pressure x-ray diffraction using rapid compression and decompression. *Rev Sci Instrum* 86:072208.
52. Lin C, et al. (2017) Kinetically controlled two-step amorphization and amorphous-amorphous transition in ice. *Phys Rev Lett* 119:135701.
53. Handa YP, Klug DD, Whalley E (1988) Energies of the phases of ice at low temperature and pressure relative to ice Ih. *Can J Chem* 66:919–924.
54. Handa YP, Klug DD (1988) Heat-capacity and glass-transition behavior of amorphous ice. *J Phys Chem* 92:3323–3325.
55. Christian JW (2002) *The Theory of Transformation in Metals and Alloys* (Pergamon, Oxford).
56. Avrami M (1939) Kinetics of phase change. I. General theory. *J Chem Phys* 7: 1103–1112.
57. Avrami M (1940) Kinetics of phase change. II. Transformation-time relations for random distribution of nuclei. *J Chem Phys* 8:212–224.
58. Liu F, Sommer F, Bos C, Mittemeijer EJ (2007) Analysis of solid state phase transformation kinetics: Models and recipes. *Int Mater Rev* 52:193–212.
59. Hallbrucker A, Mayer E, Johari GP (1989) Glass-liquid transition and the enthalpy of devitrification of annealed vapor-deposited amorphous solid water—A comparison with hyperquenched glassy water. *J Phys Chem* 93:4986–4990.
60. Angell CA (2007) Glass transition dynamics in water and other tetrahedral liquids: ‘Order-disorder’ transitions versus ‘normal’ glass transitions. *J Phys Condens Matter* 19:205112.
61. Rao CNR, Rao KJ (1978) Various kinds of phase transitions. *Phase Transitions in Solids* (McGraw-Hill, New York), pp 81–155.
62. Hage W, Hallbrucker A, Mayer E, Johari GP (1994) Crystallization kinetics of water below 150 K. *J Chem Phys* 100:2743–2747.
63. Doremus RH (1985) Diffusion and phase change. *Rates of Phase Transformations* (Academic, New York), pp 4–31.
64. Hage W, Hallbrucker A, Mayer E, Johari GP (1995) Kinetics of crystallizing D<sub>2</sub>O water near 50 K by Fourier-transform infrared-spectroscopy and a comparison with the corresponding calorimetric studies on H<sub>2</sub>O water. *J Chem Phys* 103:545–550.
65. Angell CA (1991) Relaxation in liquids, polymers and plastic crystals—Strong fragile patterns and problems. *J Non-Cryst Solids* 131:13–31.
66. Ito K, Moynihan CT, Angell CA (1999) Thermodynamic determination of fragility in liquids and a fragile-to-strong liquid transition in water. *Nature* 398:492–495.
67. Bergman R, Swenson J (2000) Dynamics of supercooled water in confined geometry. *Nature* 403:283–286.
68. Xu LM, et al. (2009) Appearance of a fractional Stokes-Einstein relation in water and a structural interpretation of its onset. *Nat Phys* 5:565–569.
69. Mallamace F, et al. (2010) Transport properties of glass-forming liquids suggest that dynamic crossover temperature is as important as the glass transition temperature. *Proc Natl Acad Sci USA* 107:22457–22462.
70. Liu L, Chen SH, Faraone A, Yen CW, Mou CY (2005) Pressure dependence of fragile-to-strong transition and a possible second critical point in supercooled confined water. *Phys Rev Lett* 95:117802.
71. Tanaka H (2003) Possible resolution of the Kauzmann paradox in supercooled liquids. *Phys Rev E Stat Nonlin Soft Matter Phys* 68:011505.
72. Chong SH (2008) Connections of activated hopping processes with the breakdown of the Stokes-Einstein relation and with aspects of dynamical heterogeneities. *Phys Rev E Stat Nonlin Soft Matter Phys* 78:041501.
73. Kawasaki K (1994) Stochastic-model of slow dynamics in supercooled liquids and dense colloidal suspensions. *Phys A* 208:35–64.
74. Bhattacharyya SM, Bagchi B, Wolynes PG (2005) Bridging the gap between the mode coupling and the random first order transition theories of structural relaxation in liquids. *Phys Rev E Stat Nonlin Soft Matter Phys* 72:031509.
75. Chang I, Sillescu H (1997) Heterogeneity at the glass transition: Translational and rotational self-diffusion. *J Phys Chem B* 101:8794–8801.
76. Swallen SF, Bonvallet PA, McMahon RJ, Ediger MD (2003) Self-diffusion of tris-naphthylbenzene near the glass transition temperature. *Phys Rev Lett* 90:015901.
77. Mapes MK, Swallen SF, Kearns KL, Ediger MD (2006) Isothermal desorption measurements of self-diffusion in supercooled o-terphenyl. *J Chem Phys* 124:054710.
78. Mapes MK, Swallen SF, Ediger MD (2006) Self-diffusion of supercooled o-terphenyl near the glass transition temperature. *J Phys Chem B* 110:507–511.
79. Chathoth SM, Damaschke B, Koza MM, Samwer K (2008) Dynamic singularity in multicomponent glass-forming metallic liquids. *Phys Rev Lett* 101:037801.
80. Zöllmer V, Rätzke K, Faupel F, Meyer A (2003) Diffusion in a metallic melt at the critical temperature of mode coupling theory. *Phys Rev Lett* 90:195502.
81. Tang XP, Geyer U, Busch R, Johnson WL, Wu Y (1999) Diffusion mechanisms in metallic supercooled liquids and glasses. *Nature* 402:160–162.
82. Knorr K, Macht MP, Freitag K, Mehrer H (1999) Self-diffusion in the amorphous and supercooled liquid state of the bulk metallic glass Zr<sub>46.75</sub>Ti<sub>18.25</sub>Cu<sub>7.5</sub>Ni<sub>10</sub>Be<sub>27.5</sub>. *J Non-Cryst Solids* 250:669–673.
83. Fielitz P, Macht MP, Naundorf V, Froberg G (1999) Diffusion in ZrTiCuNiBe bulk glasses at temperatures around the glass transition. *J Non-Cryst Solids* 250:674–678.
84. Geyer U, et al. (1995) Atomic diffusion in the supercooled liquid and glassy states of the Zr<sub>41.2</sub>Ti<sub>13.8</sub>Cu<sub>12.5</sub>Ni<sub>10</sub>Be<sub>22.5</sub> alloy. *Phys Rev Lett* 75:2364–2367.
85. Geyer U, et al. (1996) Small atom diffusion and breakdown of the Stokes-Einstein relation in the supercooled liquid state of the Zr<sub>46.7</sub>Ti<sub>18.3</sub>Cu<sub>7.5</sub>Ni<sub>10</sub>Be<sub>27.5</sub> alloy. *Appl Phys Lett* 69:2492–2494.
86. Peng Y, et al. (2015) Two-step nucleation mechanism in solid-solid phase transitions. *Nat Mater* 14:101–108.
87. Levitas VI, Henson BF, Smilowitz LB, Asay BW (2004) Solid-solid phase transformation via virtual melting significantly below the melting temperature. *Phys Rev Lett* 92: 235702.
88. Sanz E, Valeriani C (2015) Crystal-crystal transitions: Mediated by a liquid. *Nat Mater* 14:15–16.
89. Pogatscher S, Leutenegger D, Schawe JEK, Uggowitzer PJ, Löffler JF (2016) Solid-solid phase transitions via melting in metals. *Nat Commun* 7:11113.
90. Lin C, et al. (2017) A metastable liquid melted from a crystalline solid under decompression. *Nat Commun* 8:14260.
91. Skinner LB, Benmore CJ, Neuefeind JC, Parise JB (2014) The structure of water around the compressibility minimum. *J Chem Phys* 141:214507.
92. Winkel K, et al. (2008) Structural transitions in amorphous H<sub>2</sub>O and D<sub>2</sub>O: The effect of temperature. *J Phys Condens Matter* 20:494212.
93. Seidl M, Amann-Winkel K, Handle PH, Zifferer G, Loerting T (2013) From parallel to single crystallization kinetics in high-density amorphous ice. *Phys Rev B* 88:174105.
94. Shephard JJ, Klotz S, Vickers M, Salzmann CG (2016) A new structural relaxation pathway of low-density amorphous ice. *J Chem Phys* 144:204502.
95. Errington JR, Debenedetti PG (2001) Relationship between structural order and the anomalies of liquid water. *Nature* 409:318–321.
96. Hrubciak R, Sinogeikin S, Rod E, Shen G (2015) The laser micro-machining system for diamond anvil cell experiments and general precision machining applications at the High Pressure Collaborative Access Team. *Rev Sci Instrum* 86:072202.
97. Mao HK, Xu J, Bell PM (1986) Calibration of the ruby pressure gauge to 800-kbar under quasi-hydrostatic conditions. *J Geophys Res* 91:4673–4676.
98. Yen J, Nicol M (1992) Temperature-dependence of the ruby luminescence method for measuring high-pressures. *J Appl Phys* 72:5535–5538.
99. Sinogeikin SV, et al. (2015) Online remote control systems for static and dynamic compression and decompression using diamond anvil cells. *Rev Sci Instrum* 86: 072209.
100. Prescher C, Prakash VB (2015) DIOPTAS: A program for reduction of two-dimensional X-ray diffraction data and data exploration. *High Press Res* 35:223–230.